RSC Advances

PAPER

View Article Online
View Journal | View Issue

Cite this: *RSC Adv.*, 2023, **13**, 15856

Selenium-transition metal supported on a mixture of reduced graphene oxide and silica template for water splitting†

R. S. Amin,[a] Amani E. Fetohi,[a] D. Z. Khater,[a] Jin Lin,[b] Yanzhong Wang,[b] Chao Wang[b] and K. M. El-Khatib *[a]

Exploration of economical, highly efficient, and environment friendly non-noble-metal-based electrocatalysts is necessary for hydrogen and oxygen evolution reactions (HER and OER) but challenging for cost-effective water splitting. Herein, metal selenium nanoparticles (M = Ni, Co & Fe) are anchored on the surface of reduced graphene oxide and a silica template (rGO-ST) through a simple one-pot solvothermal method. The resulting electrocatalyst composite can enhance mass/charge transfer and promote interaction between water molecules and electrocatalyst reactive sites. $NiSe_2$/rGO-ST shows a remarkable overpotential (52.5 mV) at 10 mA cm^{-2} for the HER compared to the benchmark Pt/C E-TEK (29 mV), while the overpotential values of $CoSeO_3$/rGO-ST and $FeSe_2$/rGO-ST are 246 and 347 mV, respectively. The $FeSe_2$/rGO-ST/NF shows a low overpotential (297 mV) at 50 mA cm^{-2} for the OER compared to RuO_2/NF (325 mV), while the overpotentials of $CoSeO_3$-rGO-ST/NF and $NiSe_2$-rGO-ST/NF are 400 and 475 mV, respectively. Furthermore, all catalysts indicate negligible deterioration, indicating better stability during the process of HER and OER after a stability test of 60 h. The water splitting system composed of $NiSe_2$-rGO-ST/NF||$FeSe_2$-rGO-ST/NF electrodes requires only ~1.75 V at 10 mA cm^{-2}. Its performance is nearly close to that of a noble metal-based Pt/C/NF||RuO_2/NF water splitting system.

Received 24th March 2023
Accepted 18th May 2023

DOI: 10.1039/d3ra01945d

rsc.li/rsc-advances

1. Introduction

Water electrolysis is considered a zero-carbon approach for producing hydrogen; hence there is no consumption of fossil fuels or CO_2 emissions.[1] Hydrogen is a clean and efficient energy source that may be used to generate electricity in the stationary industrial and domestic and automotive sectors.[2–4] There are two main approaches for low temperature water electrolysis: liquid alkaline using a KOH electrolyte and polymer electrolyte membrane using a solid ion exchange membrane, depending on the kind of electrolyte. The most applicable kind of both is the alkaline one. This technology is designed for long-term stable operation.[5] Water electrolysis is an electrochemical process that involves two half–cell reactions: hydrogen evolution reaction (HER) and oxygen evolution reaction (OER). Because of the high energy barrier for H^+ reduction and O_2 oxidation in a water molecule, the efficiency of both processes is very low. As a direct result, the development of various kinds of electrocatalysts to facilitate both reactions is a very important issue.[6–9] Nowadays, the most efficient electrocatalysts for water electrolysis are the noble metals Ir or Ru[10] and their oxides for OER,[11] and Pt for HER.[6] However, noble metals are very rare and expensive.[12] Therefore, exploring low cost and efficient electrocatalysts is vital for water electrolysis technology.[13,14] Transition metal-based electrocatalysts, such as oxides,[15] hydroxides,[16] carbides,[17] phosphides,[18] sulfides,[19] and chalcogenides,[20] are considered promising electrocatalysts to replace noble-metal ones. Transition-metal selenides have important applications in electrochemical systems and have attracted extensive attention in water electrolysis, owing to their chemical stability, high conductivity, and efficient catalytic activity.[21,22]

It is well known that nickel and iron diselenide electrocatalysts have good performance in water-splitting reactions.[23,24] Lingling Zhai *et al.*[25] have prepared $NiSe_2$ supported on carbon fiber paper by pyrolysis and selenization reactions, the electrocatalyst exhibited overpotential values of 145 and 280 mV at a current density of 10 mA cm^{-2} for HER and OER respectively in an alkaline medium,. Moreover, iron-doping $NiSe_2$ supported on Ni–Fe foam is synthesized by Changqin Zhang *et al.*[26] by oxalic immersion and selenization method. The overpotential is 145 mV for HER and 135 mV for OER. Jing Yu *et al.*[27] prepared a P-$NiSe_2$@N-CNTs/NC hybrid catalyst that is prepared by phosphorization and selenization, with an overpotential of 95 and 306 mV gained at 10 mA cm^{-2} for HER and OER

[a]*Chemical Engineering Department, Engineering Research and Renewable Energy Institute, National Research Centre, 33 El-Buhouth St., Dokki, Cairo 12622, Egypt. E-mail: kamelced@hotmail.com*

[b]*School of Materials Science and Engineering, North University of China, Taiyuan 030051, China*

† Electronic supplementary information (ESI) available. See DOI: https://doi.org/10.1039/d3ra01945d

respectively in alkaline media. Furthermore, the hydrothermal method used to prepare $FeSe_2$ nanoparticles embedded in a selenium matrix by Fanjun Kong *et al.*[28]. They tested its electrochemical performance for OER in an alkaline medium and they found that Tafel slopes of $FeSe_2$ and $FeSe_2$@Se-2 are 70 and 54 mV dec^{-1} respectively. Tafel slope is a measure of the overall kinetics of HER and OER so a lower slope means a faster reaction. Huixuan Zhang *et al.*[24] prepared $FeSe_2/CoFe_2O_4$ by two steps hydrothermal method, it gained a Tafel slope of 88.76 mV dec^{-1} and that of $FeSe_2$ is 107.9 mV dec^{-1} for HER in an acidic medium. In addition, X. Xing *et al.*[29] found an easy way to synthesize bimetallic transition metal selenides electrocatalysts for water-splitting reactions, they prepared $FeSe_2$/CoSe nanosheet by hydrothermal and selenization processes and tested it in an alkaline medium for water electrolysis. The results reviled that, at 10 mA cm^{-2}, low overpotential of 73 mV for HER and 183 mV for OER. Moreover, Beibei Sun *et al.*[30] prepared MnS_x-Se_{1-x}@N,F-CQDs using microwave-assisted heating, hydrothermal and calcination and tested it as bifunctional electrocatalyst for water electrolysis in an alkaline medium. They found that the overpotential at 10 mA cm^{-2} of 209 mV for OER and 87 mV for HER. Xiaowei Pan *et al.*[31] developed a $CoSe_2$ nanorods and selenium vacancies using a plasma cleaner ($CoSe_2$–VSe/CC) to enhance their catalytic activity. The catalyst exhibited a lower overpotential of 88 mV at 10 mA cm^{-2} in 1 M KOH and high durability over 100 h at 100 mA cm^{-2}.

In another point of view, $CoSeO_3$ which is a transition metal selenite, has gained great interest in lithium-ion batteries.[32] Moreover, $CoSe_2/CoSeO_3$ is tested as an electrocatalyst in dye-sensitized solar cells, it is obtained by a micro emulsion-assisted hydrothermal synthesis.[33] ZHAO Dong-Jiang *et al.*[34] prepared $CoSeO_3$ nanoparticles by low-temperature refluxing method, they found that the electrocatalyst has good electrocatalytic activity towards oxygen reduction reaction. Yu Zhou *et al.*[35] synthesized a Ni–Co_4S_3 (Sv)/N-V_2CT_x electrocatalysts by sulfuration and ultrasonic treatment, the performance shows that the electrocatalyst has an overpotential of 127 mV at 10 mA cm^{-2} for HER.

To further enhance the electrochemical efficiencies of the prepared electrocatalysts towards water splitting, reduced graphene oxide (rGO), is utilized as a support material. rGO has a lot of good characteristics as low electrical resistance, high stability, and large surface area.[36] Another potential support material is hollow silica spheres; it has a mesoporous structure which enables it to be used in catalysis and drug storage applications. In this paper, reduced graphene oxide and silica templates were prepared and used as supporting materials for the electrocatalysts, $NiSe_2$, $FeSe_2$, and $CoSeO_3$ synthesized by hydrothermal technique. Integration between the supporting materials with transition metal-diselined ($NiSe_2$ and $FeSe_2$) and a transition metal selenite ($CoSeO_3$) has occurred. The prepared electrocatalysts have been tested for water-splitting reactions in an alkaline medium.

In this study, we report a one-pot solvo thermal method synthesis strategy to prepare a bifunctional electrocatalyst composed of Se and transition metals (*i.e.* Co, Ni, and Fe) supported on a mixture of rGO & ST. The atomic ratio of selenium to the other transition metals is calculated to be 1 : 1 where the total loading of the electrocatalysts on the support is fixed at 30%. The benefits of integrated structural design in delivering remarkable bi-functional activities for HER/OER. A water-splitting system composed of $NiSe_2$-rGO-ST/NF||$FeSe_2$-rGO-ST/NF electrodes requires only ~1.75 V at 10 mA cm^{-2}. Its performance is comparable to that of a noble metal-based Pt/C/NF||RuO_2/NF water splitting system. Our research demonstrates a simple method for creating bifunctional electrocatalysts for hydrogen production.

2. Materials & methods

2.1. Materials

All chemicals are obtained in analytical grade from Sigma-Aldrich (USA) and are used without any purification. All aqueous solutions, including preparation and cleaning, are made using double-distilled water.

2.2. Support preparation

2.2.1. Graphene oxide preparation. Graphene oxide (GO) is prepared following a modified Hummers' method as shown in Scheme 1.[37] 5 g of graphite powder is put in a round flask (capacity is 2000 mL) then 360 mL of concentrated H_2SO_4 and 40 mL of phosphoric acid are added to the graphite under stirring at room temperature for one hour. Afterward, the round

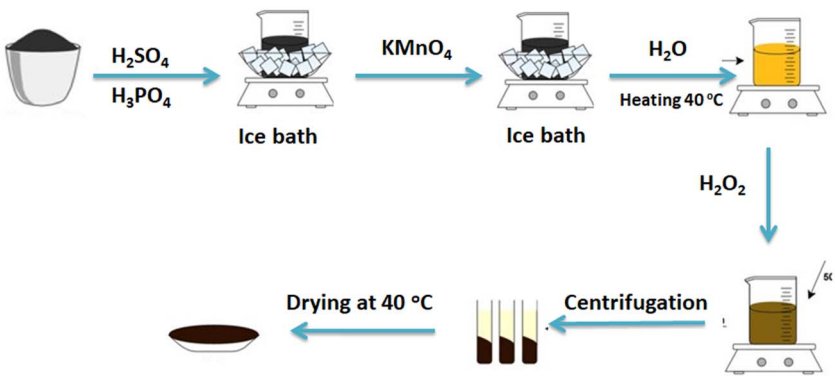

Scheme 1 Procedure of graphene oxide preparation.

flask is placed in an ice bath. After cooling, the mixture of 18 g of potassium permanganate is added slowly under continuous stirring (1 g each 10 min). After finishing the addition of potassium permanganate powder, the mixture remains in the ice bath for 10 minutes. Then the produced mixture is warmed up to 40 °C and maintained at this temperature for two and half hours in a water bath resulting in a thick paste. Subsequently, an additional 500 mL of water is followed by the addition of 30 mL of hydrogen peroxide (30%). Afterward, 250 mL of 10% hydrochloric acid is added to the mixture. Lastly, the mixture is rinsed and centrifuged many times to eliminate supernatant contaminants until the pH of the supernatant water reaches 5.5. Then the mixture is dried in a hot air oven at 80 °C for six hours.

2.2.2. Silica template preparation. The silica template is synthesized by mixing ammonia-catalyzed hydrolysis of tetraethoxysilane (TEOS) in ethanol–water solvents.[38] The procedure of preparation is as follows: 8 mL of double-distilled water and 8 mL of ammonia are added into 200 mL of ethanol mixed with 10 mL of TEOS solution. The mixture is stirred continuously for 24 hours then it is filtered and dried in a dryer at 80 °C for 6 hours.

2.2.3. Mixed GO and silica template support preparation. An appropriate amount of prepared graphene oxide is added to a 200 mL aqueous solution of ST under intense magnetic stirring for 1 h. The product is obtained by filtration and washing with double distilled water. The resulting mixture dried in a dryer at 80 °C for 6 h.

2.3. Preparation of selenium-transition metal supported on a mixture of rGO and ST

The electrocatalysts are prepared using the one-pot solvo thermal method as shown in Scheme 2. The bimetallic electrocatalysts are composed of Se and transition metals (*i.e.* Co, Ni, and Fe) supported on a mixture of rGO & ST. The atomic ratio of selenium to the other transition metals is calculated to be 1 : 1 where the total loading of the electrocatalysts on the support is fixed at 30%. Chloride salts are used as the precursors for the transition metals. For a typical synthesis, appropriate amounts of Se and $NaBH_4$ (it acted as a reducing agent) are dissolved into 50 mL *N*,*N*-dimethyl formamide (DMF). The mixture is then agitated until a uniformly distributed black-color solution is formed. Afterward, calculated amounts of metal chlorides are added to this black-color solution. The produced solution is then placed in a Teflon-lined autoclave and heated at 160 °C for 24 hours. After cooling naturally, the acquired products are filtrated and washed with double distilled water several times and dried in a dryer at 60 °C for 6 hours. According to the procedure mentioned above, the electrocatalysts prepared are namely as follows: $CoSeO_3$/rGO-ST, $NiSe_2$/rGO-ST, and $FeSe_2$/rGO-ST.

2.4. Physical characterization of the electrocatalysts

The crystalline phase is analyzed *via* a Rigaku-D/MAX-PC 2500 X-ray diffraction (XRD) system. Scanning electron microscopy (SEM) and high-resolution transmission electron microscopy (HRTEM, JEOL-JEM 2010) are utilized to investigate microstructure and morphology. X-ray photoelectron spectroscopy (XPS) (PH1-5700 ESCA system, US) is used to determine the valence states of the electrocatalyst.

2.5. Electrochemical characterization

2.5.1. Electrode preparation. The catalyst and polyvinylidene fluoride (PVDF) are blended in *N*-methyl-2-pyrrolidone (NMP) solvent with a ratio of 9 : 1 by weight to obtain catalyst slurry. Then, the mixture is treated by sonication for more than 1 h until the slurry becomes a uniform dispersion nickel foam (1 cm × 2 cm) is cleaned by sonication in HCl (3 M) for 15 min, deionized water, and ethanol, respectively, and then dried in a vacuum oven at 60 °C for 8 h. The slurry is drop cast on glassy carbon 3 mm diameter (0.07 cm^2) for hydrogen evolution reaction, and 1 × 1 cm^2 nickel foam to make a working electrode for oxygen evolution reaction (the loading mass is about 1 mg cm^{-2}).

2.5.2. Electrochemical characterization of electrocatalyst. The electrocatalytic activities are evaluated using a three-electrode setup equipped with an electrochemical workstation Voltalab6. The counter electrode and reference electrodes are platinum wire and a KCl-saturated Ag/AgCl electrode, respectively. Polarization curves for HER and OER are measured using

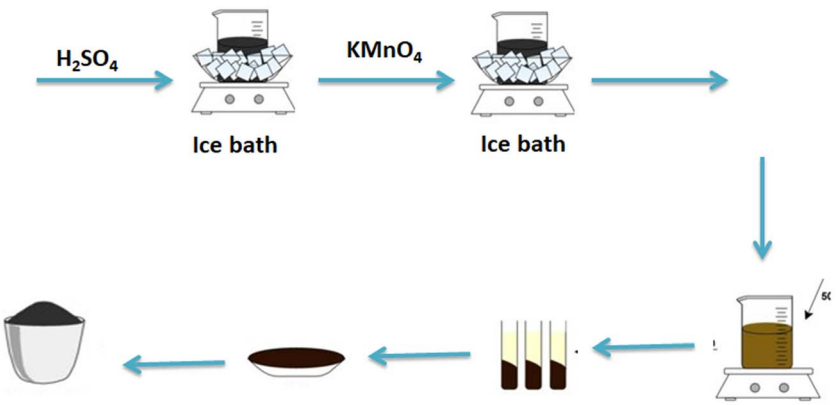

Scheme 2 Procedure of selenium-transition metal supported on rGO and ST preparation.

linear sweep voltammetry (LSV) at a scan rate of 5 mV s^{-1} in 1.0 M KOH and corrected with *iR* compensation. Electrochemical impedance spectroscopy (EIS) measurement is performed in a frequency range of 0.1–10^5 Hz with a polarized potential in the turnover region of the HER and OER. All potentials are corrected to the reversible hydrogen electrode (RHE) according to the Nernst equation: $E_{RHE} = E(Ag/AgCl) + 0.197 + 0.059 \times pH$. The electrochemically active surface areas (ECSA) of as-obtained electrocatalysts are achieved from the corresponding electrochemical double-layer capacitance (C_{dl}), which can be calculated from CV curves. Cyclic voltammograms (CV) are recorded with increasing scan rates (20–140 mV s^{-1}) within the non-faradaic potential region (0.67–0.77 V *vs* RHE) for HER & (1.2–1.3 V *vs.* RHE) for OER.

3. Results & discussion

3.1. Physical characterization

3.1.1. Physical characterization of support. The X-ray powder diffraction patterns of the ST, graphene, and graphene oxide combined with the ST are represented in Fig. 1(a). Regarding the XRD pattern of ST, it showed a single broad reflection at 2θ around 22°, and that is equivalent to the average pore–pore correlation distance in the small-angle region, which is consistent with the mesoporous structures of the silica spheres.[39] The XRD pattern of graphene oxide reflected two peaks at 2θ equal to 10.41° and 42.49°. The sharp peak at 10.41° representing the (001) GO layers the oxidation of graphite is confirmed by this diffraction peak that indicated the presence of oxygen-rich functional groups.[40,41] The 42.49° diffraction peak corresponds to the (101) crystallographic planes of graphitic materials.[42] The XRD pattern of the mixed support (GO and ST) reflected three diffraction peaks at 2θ equal to 10.09°, 22.57°, and 42.65° and this confirmed the presence of both supports, it could be noticed that the intensity of (001) GO peak is decreased because the presence of ST that covered the surface of GO (this will be further confirmed by TEM analysis).

The morphology and particle distribution of different prepared supports and electrocatalysts are determined using TEM analysis. Fig. 1(b–g) represents the TEM images of the GO (b and c), silica template (d and e), and a mixture of both (f and g) under different magnifications. GO showed a tulle-like structure, typically smooth and wrinkled across its surface owing to its oxygenated functional groups.[43] It can also be seen that the mono- or multi-layered GO particles are created using thin semi-transparent sheets.[44] Furthermore, TEM images of GO have transparent sheet structures.[42] It could be noticed that obtained GO is composed of a smooth planar structure with thin individual layers. However, the areas in GO images that have lower brightness may be attributed to the elastic corrugations.[45]

Fig. 1(d and e) represents TEM images of silica samples, revealing that the obtained silica particles are mesoporous; however, neither uniform morphology nor is ordered mesostructure achieved. TEM images confirmed the formation of partially-bridged hollow nanospheres.[46] Moreover, the SiO_2 material is composed of round-shape particles on their surface with smaller-sized particles.[47] The mixed support of GO and silica templates TEM images are displayed in Fig. 1(f and g). It is noticed that the presence of apertures and slits on the GO surface is an indication of the existence of silica. A higher magnification image of the mixed support showed the dispersal of mesoporous silica on the outer surfaces of the GO (Fig. 1g) indicating good dispersion of silica particles on the graphene oxide surface.

The XPS analyses of the mixed support rGO-ST are shown in Fig. 2(h–j). The C 1s XPS spectra (292.18–281.88 eV) could be

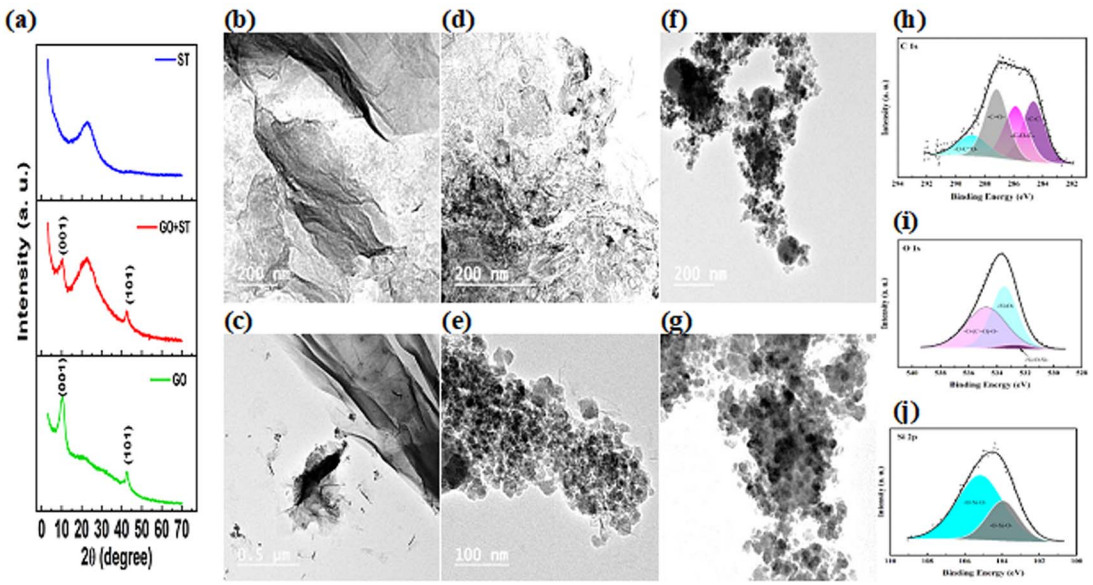

Fig. 1 (a) XRD pattern of ST, rGO and rGO-ST, HR-TEM images of the GO (b and c), silica template (d and e), and rGO-ST (f and g), high-resolution XPS spectra of the C 1s (h), O 1s (i), and Si 2p (j) on the surface of the mixed support rGO-ST.

deconvoluted into four peaks that attributed to the C–C, C–O–C, O–C=O, and C=O at binding energies of 284.63, 285.86, 288.88 and 287.18 eV, respectively as shown in Fig. 2(h). The O 1s is also deconvoluted into three peaks at 533.48, 532.95, and 534.74 eV that are assigned to Si–OH, Si–O–Si, and O–(C=O)–O, respectively, as indicated in Fig. 2(i).[48] To further investigate the bonding mode of Si in the support material, the high-resolution Si 2p (109.08–100.68 eV) spectrum is deconvoluted into two peaks at 103.94 and 105.17 eV as illustrated in Fig. 2(j), they are ascribed to SiO_2. These results imply the doping of ST in the rGO.[49]

3.1.2. Physical characterization of electrocatalyst. Fig. 2(a) illustrated the XRD patterns of prepared selenium-transition metals supported on mixed rGO and ST, it could be noticed that there is not any obvious peak of GO, rGO, or ST in the XRD patterns. We could say that after hydrothermal reaction GO is reduced to rGO or this may be due to the presence of transition metal particles on the surface of the support material that indicates the complete coverage of the surface with the electrocatalysts particles. Furthermore, there are no diffraction peaks of any impurities in all the XRD curves which reflected the formation of a pure phase of prepared electrocatalysts. The diffraction peaks of the $FeSe_2$ XRD diffraction curve are completely consistent with the orthorhombic $FeSe_2$. Peaks at around 23.83°, 29.25°, 31.07°, 34.75°, 36.07°, 48.08°, 49.00°, 53.82, 57.37°, 59.65° and 64.02° can be marked as diffraction

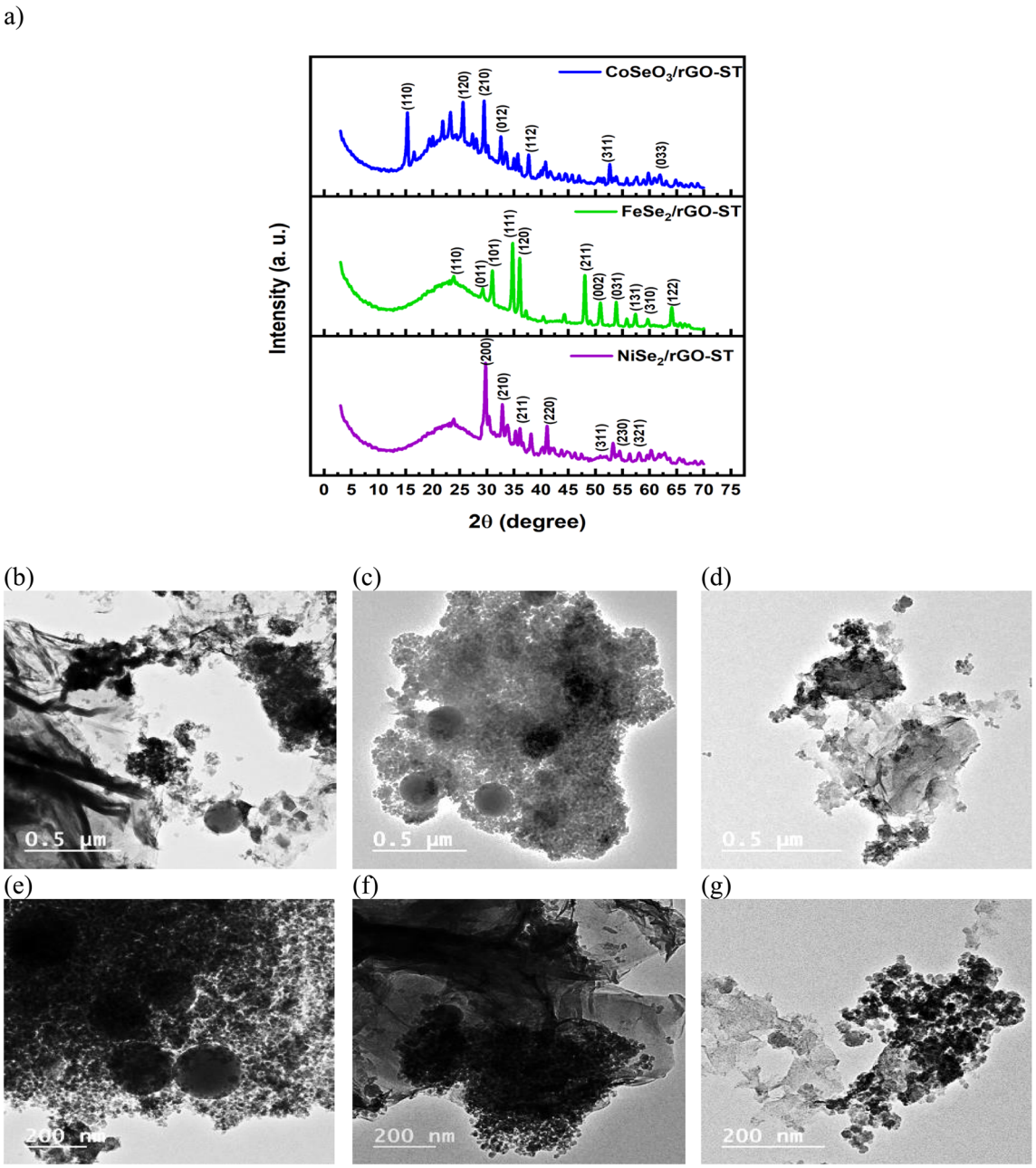

Fig. 2 XRD analysis of the electrocatalyst (a), HR-TEM analysis of $NiSe_2$/rGO-ST (b and c), $CoSeO_3$/rGO-ST (d and e), and FeS_2/rGO-ST (f and g).

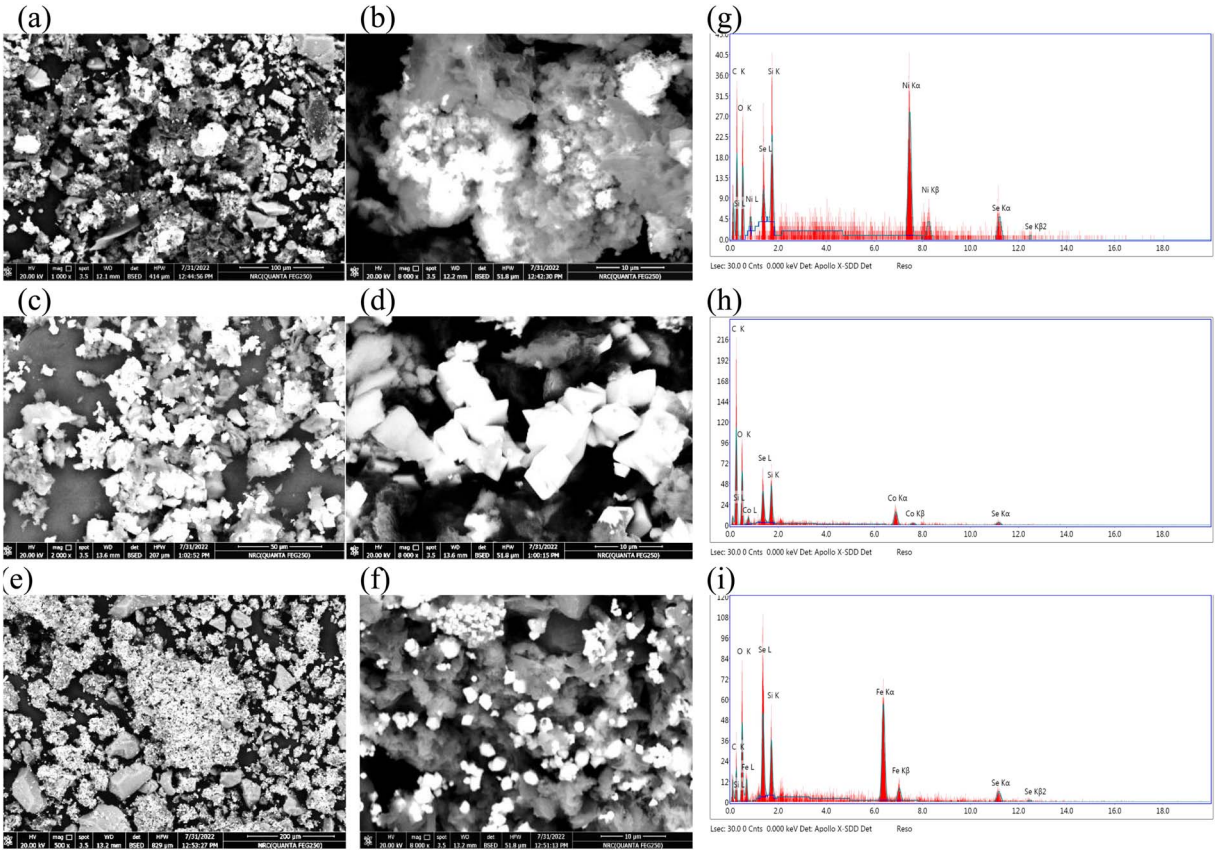

Fig. 3 SEM & EDAX analysis of $NiSe_2$/rGO-ST (a, b and g), $CoSeO_3$/rGO-ST (c, d and h), and $FeSe_2$/rGO-ST (e, f and i).

peaks of the orthorhombic $FeSe_2$ (110), (011), (101), (111), (120), (211), (002), (031), (131), (310) and (122), respectively.[50] $NiSe_2$ electrocatalysts displayed the diffraction peaks at 2θ of 29.86°, 33.79°, 36.79°, 42.43°, 50.56°, 55.30°, and 57.25°, those peaks are standard for the (200), (210), (211), (220), (311), (230) and (321) crystal planes.[51] Regarding the diffraction curve of $CoSeO_3$, it had main characteristic peaks at 15.38°. 25.62°, 29.53°, 32.64°, 37.67°, and 52.63° are all observed and matched well with the crystal planes of (110), (120), (210), (012), (112), (311), and (033).[52]

TEM analysis of $NiSe_2$, $CoSeO_3$, and FeS_2 supported on rGO-ST are performed, and their results are presented in Fig. 2(b–g) respectively, all the nanoparticles are quite fine (around 20 nm in size) where each nanocrystal is connected tightly with its neighboring,[53] the nanocrystals are composed of irregularly shaped nanoparticles that distributed homogenously on the rGO-ST support. It is also noticed that the ST particles are shown in the form of large dark gray circles furthermore, the wrinkles of reduced graphene could also be observed in all samples indicating well hybridization with MSe_x nanoparticles.[54] Heavy distribution of nanoparticles on the mixed support is observed for $NiSe_2$/rGO-ST and $CoSeO_3$/rGO-ST while it is not the case in FeS_2/rGO-ST images where there are larger areas of the support without the electrocatalysts nanoparticles. It is well known that nano-scale size and the coverage of the nanoparticles on the support in a dense way provide multiple catalytic sites.

Fig. 3(a–f) represents the SEM images of different electrocatalysts, by reference to the morphology of prepared electrocatalysts, lots of nanoparticles could be easily observed on the substrate, and those particles are stacked together. These nanoparticles are in the form of nanospheres for $NiSe_2$/rGO-ST (a and b). Min Zhu *et al.*[55] synthesized Fe-doped $NiSe_2$ nanospheres supported on reduced graphene oxide through low-temperature reflux and solvo thermal process. They found that the presence of reduced graphene as support limits the excess growth of the nanosphere of the electrocatalysts during the synthesis procedure. Moreover, the nanospheres of $NiSe_2$ tend to agglomerate in the absence of reduced graphene. In the case of $CoSeO_3$/rGO-ST (c and d) and $FeSe_2$/rGO-ST (e and f) the particles tended to be cubes this is in agreement with Kaviyarasu[56] who prepared cubic ZnSe and Balamuralitharan *et al.*[57] who prepared $MnSe_2$ cubes. Abundant mesoporous structures are spreading all over the matrix, which increases the surface area (in agreement with TEM analysis).

Fig. 3(g–i) presents EDAX spectra and elemental composition of MSe/rGO-ST which exhibits peaks for selenium (Se), carbon(C), oxygen (O), silicon (Si), and M where M is Ni, Mn, Co, Zn, and Fe, respectively. These peaks suggest the formation of MSe/rGO-ST. The intensity of different peaks is different. The elemental analysis indicates that selenium and carbon peaks

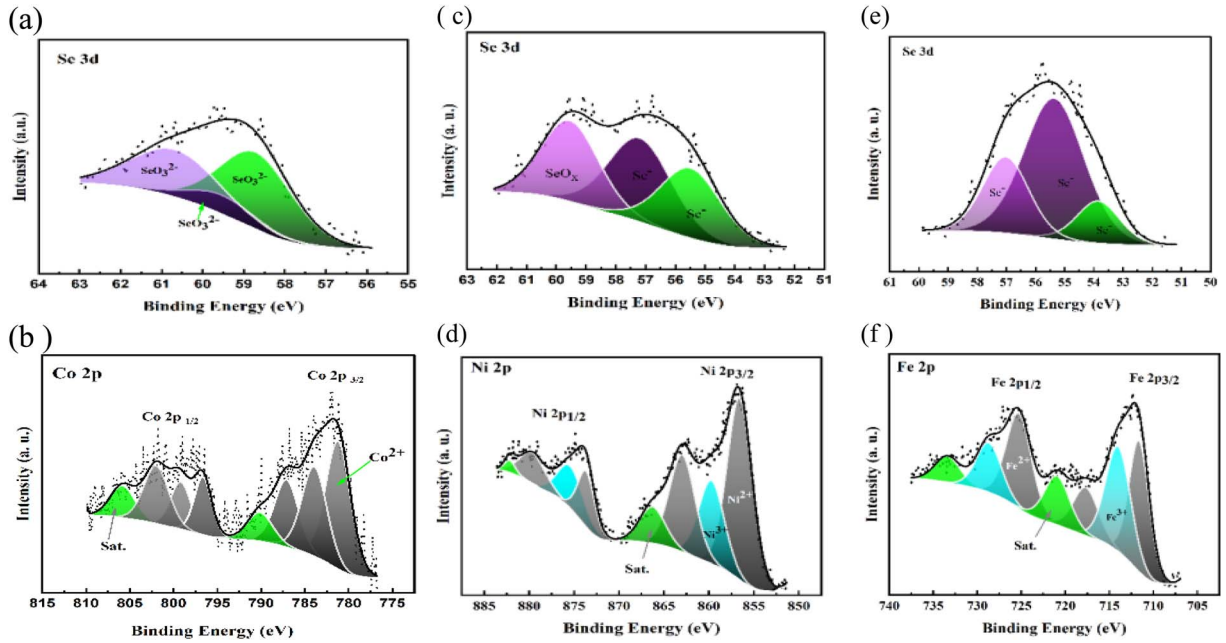

Fig. 4 XPS spectra of $CoSeO_3$/rGO-ST (a and b), $NiSe_2$/rGO-ST (c and d), and FeS_2/rGO-ST (e and f) electrocatalysts.

correspond to the substrate while oxygen peaks are from the oxygen present in the atmosphere.[58] It is also noticed that Ni has intense peaks; this is in coincidence with its corresponding elemental composition.

The stoichiometry and valences state of each electrocatalyst are further carried out using XPS analyses from the wide survey's spectra of $CoSeO_3$/rGO-ST, $FeSe_2$/rGO-ST, and $NiSe_2$/rGO-ST films that measured over a binding energy range of 0 to 1400 eV and the graphs are displayed in Fig. S1(a–c).† It could be observed that the presence of main photoemission intensity peaks appeared at ~285.95, 533.63, 104.78, 57.02, 783.13, 713.41 and 858.21 eV. The previous binding energies correspond to the C 1s, O 1s, Si 2p, Se 3d, Co2p, Fe2p, and Ni2p regions, respectively, as the main species in the as-prepared electrocatalysts. The high-resolution XPS spectra of Se 3d spectra regions for all prepared electrocatalysts are presented in

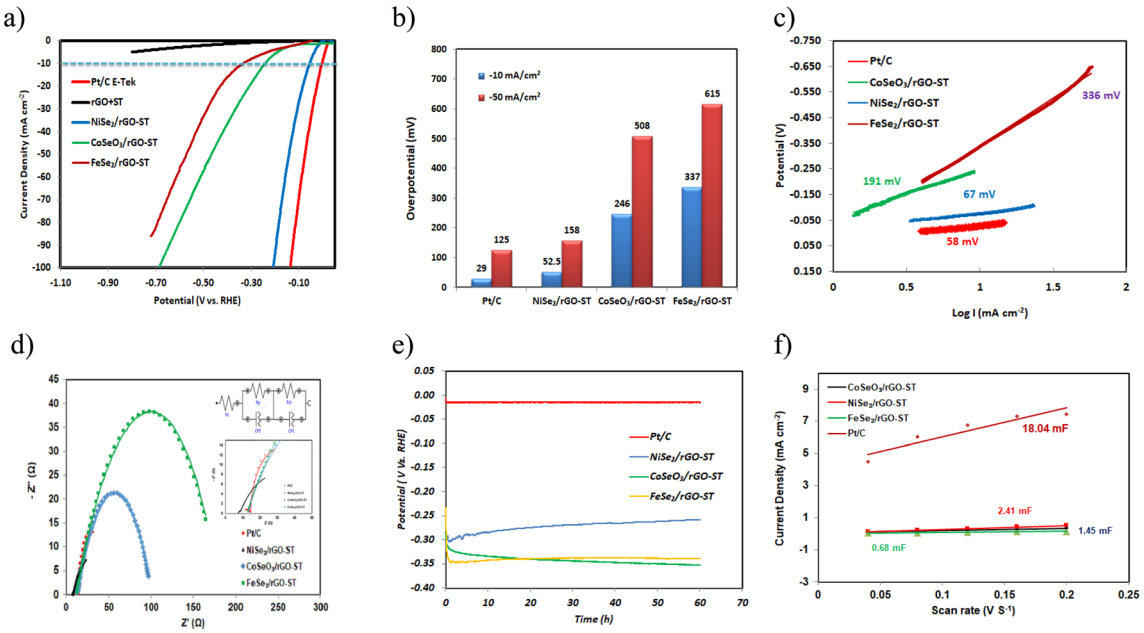

Fig. 5 OER performance of the electrocatalysts Pt/C E-TEK, $NiSe_2$/rGO-ST, $CoSeO_3$/rGO-ST and $FeSe_2$/rGO-ST. (a) LSV curves, (b) the comparison of the overpotential, (c) Tafel plots derived from LSV curves, (d) Nyquist plots, (e) chronopotentiometry (CP) curve, and (f) the double-layer capacitance (C_{dl}) plots.

Table 1 A performance comparison with recently published non-noble metal-based for HER, OER and water splitting catalysts

	HER		OER		Water electrolysis
Electrocatalyst	Overpotential η (mV)@10 mA cm^{-2}	Tafel slopes (mV dec^{-1})	Overpotential η (mV)	Tafel slopes (mV dec^{-1})	Potential (V)@10 mA cm^{-2}
$NiSe_2$/rGO-ST (this study)	52.5	67	280@20 mA cm^{-2} 400@50 mA cm^{-2}	236	$NiSe_2$-rGO-ST/2NF||$FeSe_2$-rGO-ST/NF (1.75)
$CoSeO_3$/rGO-ST (this study)	246	191	284@20 mA cm^{-2} 475@50 mA cm^{-2}	127	
$FeSe_2$/rGO-ST (this study)	347	363	229@20 mA cm^{-2} 297@50 mA cm^{-2}	106	
$NiSe_2$/CF (NSN/CFP)[25]	145	72	280@10mA cm^{-2}	81	1.66 (bifunctional)
P-$NiSe_2$@N-CNTs/NC[27]	95	82	306@10 mA cm^{-2}	61	1.61 (bifunctional)
Se–$NiSe_2$/CC[86]	133	128	350@100 mA cm^{-2}	190	1.57 (bifunctional)
TiN@NiO–$NiSe_2$/CC[87]	115	59 ± 4	240@10 mA cm^{-2}	29 ± 3	1.57 (bifunctional)
$NiSe_2$/Ni_2P@FeP[109]	113	73.1	202@10 mA cm^{-2}	42.1	1.554 (bifunctional)
Fe–$NiSe_2$/CC[110]	—	—	257@10 mA cm^{-2}	43	—
$NiSe_2$/Ni_2O_3/FeOOH[111]	—	—	270@100 mA cm^{-2}	54.7	—
10%P–$NiSe_2$/$CoSe_2$ (ref. 88)	—	—	287@50 mA cm^{-2}	68	—
$NiSe_2$/$FeSe_2$/NiFe (NFS/NFF)[23]	—	—	274@40 mA cm^{-2}	57.07	—
$Ni_{0.7}Fe_{0.3}Se_2$/rGO-30%	—	—	265@10 mA cm^{-2}	57	—
$Ni_{0.7}Fe_{0.3}Se_2$			325@10 mA cm^{-2}	70	
$NiSe_2$ (ref. 55)			422@10 mA cm^{-2}	79	
Cu-(a-$NiSe_x$/c-$NiSe_2$)/TiO_2 (ref. 85)	156.9	51.2	339@10 mA cm^{-2}	54.2	1.62 (bifunctional)
$NiSe_2$/Ni–Fe[26]	145	—	135@10 mA cm^{-2}	—	1.58 (bifunctional)
KMF_3 (M = Co/Fe)[112]	—	—	254@10 mA cm^{-2}	37.5	—
Fe_2OF_4/nickel foam[113]	—	—	238@10 mA cm^{-2}	48	—
Fe–NiCoP[114]	—	—	266@10 mA cm^{-2}	75.2	Fe–NiCoP||Pt/C 1.72
$FeSe_2$	—	—	338@10 mA cm^{-2}	139	—
$CoSe_2$			346@10 mA cm^{-2}	65	
$NiSe_2$			305@10 mA cm^{-2}	91	
$NiSe_2$/$FeSe_2$ (ref. 115)			256@10 mA cm^{-2}	50	
$FeSe_2$–$CoSe_2$/$CoSe_2$ (ref. 116)	—	—	260@10 mA cm^{-2}	51.3	—
$CoSe_2$@NSC	—	—	364@10 mA cm^{-2}	114.78	$FeSe_2$/$CoSe_2$@NSC||Pt/C
$FeSe_2$/$CoSe_2$@SC			407@10 mA cm^{-2}	110.50	1.57
$FeSe_2$/$CoSe_2$@NSC[117]			278@10 mA cm^{-2}	53.08	
Fe–Co–S/CC[89]	320	82.60	258@10 mA cm^{-2}	61.20	1.51 (bifunctional)

Fig. 4(a–c). As displayed in Fig. 4(a) in the case of $CoSeO_3$/rGO-ST, exhibited the presence of three fitted peaks at 58.7, 59.51, and 60.67 eV that is in accord with Se–O bonding structures, which indicates the presence of SeO_3^{2-} as previously illustrated.[59,60] Whereas, Fig. 4(b and c) showed that there are monovalent (Se^-) and divalent (Se^{2-}) oxidation states of selenium, in addition to the existence of SeO_x (58.29 eV) that is caused by surface oxidation.[61] As shown in $FeSe_2$/rGO-ST, the characteristic oxidation state of Se^- is assigned to binding energies of ~54.53 and ~56.6 eV.[62,63] Moreover, the atomic Se^{-2} corresponds to ~53.84 eV and 57.37 eV in the case of NiSe/rGO-ST.[56] The high-resolution XPS spectra of Co2p, Fe 2p, and Ni 2p are also separately presented in Fig. 4(d and e), respectively. The Co 2p spectrum as illustrated in Fig. 2(t) is deconvoluted into two spin–orbit doublets (Co $2p_{3/2}$ at 776.78 eV and Co $2p_{1/2}$ at 795.8 eV) along with two respective satellite peaks, as reported previously.[64,65] Besides, the occurrence of six major peaks positioned at 781.2, 798.48, 796.3, 783.91, 787.09, and 801.98 eV are correlated to Co^{2+} ions.[66] Furthermore, the prominent satellite peaks are located at 790.13 and 805.84 eV which are attributed to the coexistence of Co^{2+}.[5,67] Similarly, the Fe 2p spectrum reveals two spin–orbit doublets for Fe $2p_{3/2}$ and Fe $2p_{1/2}$ at 706.98 and 737.48 eV, respectively. The first doublet is deconvoluted at 711.62, 713.99 and 720.93 eV, indicating the presence of Fe^{2+}.[68] The second one is also deconvoluted at 717.65 and 728.67 eV which can be assigned to Fe^{3+}.[69] Moreover, the presence of two broad satellite peaks at 725.27 and 733.36 eV (Fig. 2(u)). In the case of the Ni $2p_{3/2}$ and Ni $2p_{1/2}$ spectra are correlated to the binding energies of 856.58 and 873 eV, respectively, as indicated in Fig. 4(f). In addition, the existence of shake-up satellite peaks at binding energies of 866.28 and 882.15 eV.[70,71] Furthermore, the obtained peaks at 856.58, 859.72, and 874.99 eV are accredited to Ni^{2+}.[72,73] Whereas, 862.96 and 873.23 eV are assigned to Ni^{3+}.[74–76] Ni^{3+} may be produced by the low coordination or partial oxidation of Ni ions at the surface.[77] Consequently, the Ni selenide mainly show a divalent state.

Moreover, for all specimens, to further probe the bonding mode of Si as illustrated in Fig. S2(a),† the fitted high-resolution Si 2p spectrum region is deconvoluted into two distinguishable

peaks at ~103.98 and ~105.05 eV that ascribed to –C–Si–O bond and O–Si–O bonds of SiO_2, respectively.[49] Significantly, the high-resolution C 1s spectra revealed a major peak fitted at 284.68 eV that corresponded to the C–C/C=C bonds of sp^2 hybridized graphite carbon atoms in Fig. S2(b).† Another oxygen-containing group that could be assigned to C–O, C–O–C, C=O, O–C=O chemical bonds at 286.08, 286.4, 287.64, 289.42 eV, respectively, these values are consistent with those for rGO.[78–80] The accompanying O 1s spectra manifest the coexistence of three peaks with binding energies at 530.86, 532.97, and 534.4 eV that could be attributed to the C=O, Si–O–Si, and O–(C=O)–O, respectively, that assists as a nucleus structure on the surface of rGO in Fig. S2(c).† It could be concluded that the XPS results are in line with XRD data.

3.2. HER performance

HER performance of electrocatalysts $NiSe_2$/rGO-ST, $FeSe_2$/rGO-ST, and $CoSeO_3$/rGO-ST is tested in a three-electrode system using 1 M KOH as electrolyte. For comparison, the performance of the mixed support rGO-ST and Pt/C E-TEK is also evaluated under the same conditions. The *iR*-corrected linear polarization curves (LSV) are represented in Fig. 5(a). At a current density of 10 mA cm^{-2}, $NiSe_2$/rGO-ST had an overpotential of 52 mV, which is somewhat comparable to Pt/C E-TEK (29 mV) and much smaller than those of $FeSe_2$/rGO-ST (337 mV), and $CoSeO_3$/rGO-ST (246 mV). The linear polarization curve (LSV) without *iR* correction for the electrocatalysts for HER is shown in Fig. S3(a).† Furthermore, η values at 50 mA cm^{-2} are 125, 158, 518 and 615 mV for Pt/C, $NiSe_2$/rGO-ST, $CoSeO_3$/rGO-ST, and $FeSe_2$/rGO-ST, respectively as shown in Fig. 5(b). The ESI† (rGO-ST) exhibited poor performance indicating that the improved catalytic activity is related to the metal electrocatalysts.[81] From the thermodynamics point of view, to have the same current density at lower overpotential means better performance of the electrocatalyst because of less electrical energy consumption. In addition, η value at 10 mA cm^{-2} of the $NiSe_2$/rGO-ST surpasses that of some recently reported HER catalysts in alkaline medium, for example, nickel diselenide ($NiSe_2$) anchored on carbon fiber paper (CFP) (145 mV),[82] iron-doping $NiSe_2$ nano wrinkles (145 mV),[83] copper-incorporated heterostructures of amorphous $NiSe_x$/crystalline $NiSe_2$ (156.9 mV),[84] CNTs encapsulating P-doped $NiSe_2$ nanoparticles on carbon framework (95 mV),[85] hybrid nanosheet arrays $NiSe_2$/CC-180 (133 mV),[86] NiO–$NiSe_2$ nanosheet-based heterostructures shelled titanium nitride array (115 mV),[87] $NiSe_2$/Ni_2P@FeP interface nanosheets (113 mV).[88] To the best of our knowledge, $CoSeO_3$/rGO-ST and $FeSe_2$/rGO-ST catalyzing HER have been rarely reported in the literature. However, they both have a reasonable and comparable overpotential at 10 mA cm^{-2}, for example, Xueying Li *et al.*[89] prepared different HER electrocatalysts composed of Fe–Co–S nanoflakes grew on the carbon cloth by hydrothermal method and annealing treatment, they found that at the current densities of 10 mA cm^{-2}, the overpotential of Co–S/CC, Fe–Co–S/CC-37.5, Fe–Co–S/CC-75, and Fe–Co–S/CC-150 is 330, 320, 260, and 320 mV respectively. Moreover, the Co–BTC (1,3,5-benzene tricarboxylic acid) electrocatalyst prepared by pulsed laser ablation in dimethyl formamide[90] showed an overpotential of 437 mV toward HER at a current density of 10 mA cm^{-2} in 1.0 M KOH. More performance comparison with recently published non-noble metal-based for HER catalysts is listed in Table 1.

As shown in Fig. 5(c) the outstanding HER catalytic activity of $NiSe_2$/rGO-ST is further verified by the corresponding Tafel slope of 67 mV dec^{-1} revealing a typical Volmer–Heyrovsky pathway with the Volmer step being the rate-limiting step,[91] Tafel slopes of $FeSe_2$/rGO-ST is 363 mV dec^{-1} and that of

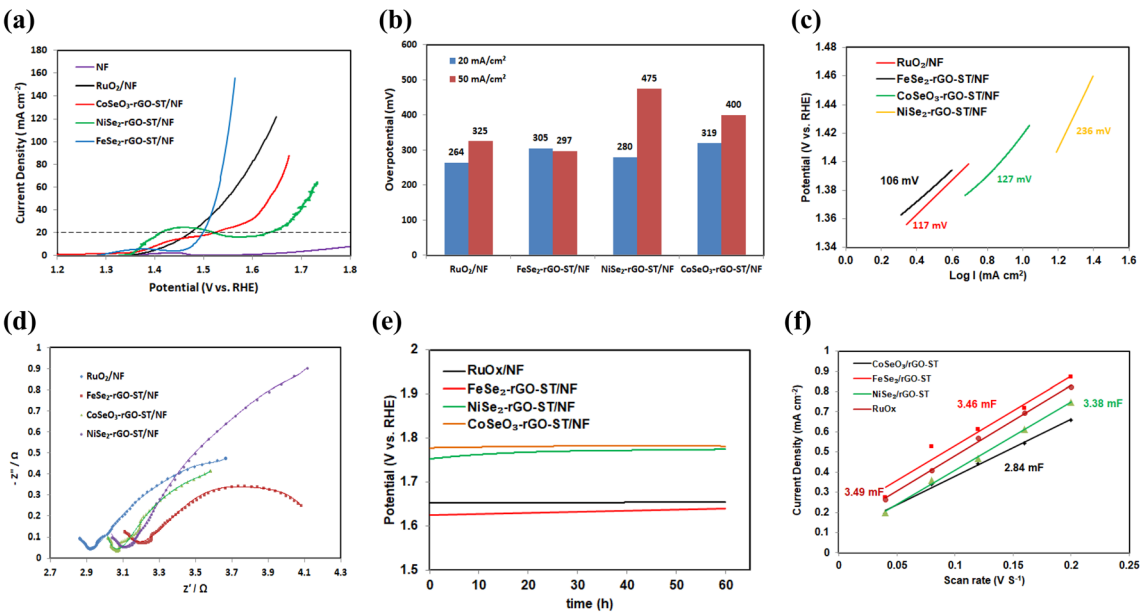

Fig. 6 OER performance of the electrocatalysts RuO_x, $NiSe_2$/rGO-ST, $CoSeO_3$/rGO-ST, and $FeSe_2$/rGO-ST. (a) LSV curves, (b) the comparison of the overpotential, (c) Tafel plots derived from LSV curves, (d) Nyquist plots, and (e) chronopotentiometry (CP) curve at 30 mA cm^{-2}.

$CoSeO_3$/rGO-ST is 191 mV dec^{-1}. The small Tafel slope of $NiSe_2$-rGO-ST will lead to a faster incrimination of the HER rate with increasing overpotential.[92]

The Nyquist plots are represented in Fig. 5(d), and equivalent circuits of the electrocatalysts are shown in the inset of Fig. 5(d). The R_s (resistance of the solution), R_{ct} (resistance of the charge transfer), and CPE (constant phase element) values are represented in Table S1.† The charge transfer resistance values (R_{ct}) are determined by the semicircular diameter in the high-frequency region.[93,94] The R_{ct} values for Pt/C E-TEK, $NiSe_2$/rGO-ST, $CoSeO_3$/rGO-ST, and $FeSe_2$/rGO-ST and are 27.29, 40.07 and 87.41, 168.90 Ω respectively in 1 M KOH. From a general point of view, small values of R_{ct} mean good contact between nano electrocatalysts and supporting materials. Moreover, $NiSe_2$/rGO-ST has the smallest R_{ct} value, in other words, it has the fastest charge transfer ability among tested electrocatalysts.[93,94]

Fig. 5(e) shows the chronopotentiometry curve of different electrocatalysts at an overpotential of −10 mV in 1 M KOH solution for 3600 s. The current density showed only a little deterioration, which might be attributed to H^+ consumption or residual H_2 bubbles on the electrode surface, which hampered the process.[81] The $NiSe_2$/rGO-ST showed the largest and the most stable current when compared to $CoSeO_3$/rGO-ST and $FeSe_2$/rGO-ST. As a result, the $NiSe_2$/rGO-ST showed superior stability for the HER in the alkaline electrolyte.

To gain further insight into HER activity, we determine the electrochemical sensitive area (ECSA) which is directly affected by the number of active sites for the HER.[95] The ECSA is calculated by measurement of the capacitance as it is linearly proportional to the double-layer capacitance (C_{dl}).[96] ECSA is calculated according to the following equation:[97]

$$\text{ECSA (cm}^2\text{)} = \text{capacitance (}\mu\text{F)/40 }\mu\text{F cm}^{-2} \quad (1)$$

The electrochemical active surface area is estimated using the simple cyclic voltammetry (CV) method. Fig. S4(a–c)† represented CVs of the prepared electrocatalysts in the potential region from (0.67 to 0.77 V *vs.* RHE) at different scan rates of 40–200 mV s^{-1}. The double-layer capacitances (C_{dl}) for each electrocatalyst are directly proportional to the surface area. It is determined by plotting $\Delta J = j_a - j_c$ at a given potential (0.72 V *vs.* RHE) against the CV scan rates and illustrated in Fig. S4†[98] in which the slope is equal to twice that of C_{dl}.[99] A linear plot with slope values of 18.04, 2.41, 1.45, and 0.68 mF cm^{-2} for Pt/C E-TEK, $NiSe_2$/rGO-ST, $CoSeO_3$/rGO-ST, and $FeSe_2$/rGO-ST, respectively as shown in Fig. 5(f). These C_{dl} values resemble those obtained by Zhu *et al.*[100] who obtained a C_{dl} value of 2.77 mF cm^{-2} for $CoSeO_3$/rGO-ST and 1.93 mF cm^{-2} for $NiSe_2$/rGO-ST.

Pt-E-TEK retained a high ECSA of 270.75 cm^2 while those of $NiSe_2$/rGO-ST, $CoSeO_3$/rGO-ST and $FeSe_2$/rGO-ST are 36.12, 14.25 and 12.32 cm^2. The superior HER catalytic performance of $NiSe_2$/rGO-ST could be due to the large electrochemically active surface area and subjected active sites.

Based on the above findings, we may conclude that $NiSe_2$/rGO-ST is a potential low-cost catalyst for the hydrogen evolution process in an alkaline medium depending on its remarkable overpotential, Tafel slope, electrochemical surface area, and stability values.

3.3. OER performance

OER activities of prepared electrocatalysts are further investigated using linear sweep voltammetry (LSV). Similar measurements are also taken for bare NF and RuO_x/NF with the same loading. Their linear sweep voltammetry (LSV) curves *vs.* the reversible hydrogen electrode (RHE) scale is shown in Fig. 4(a). All potentials shown are corrected for the ohmic potential drop, and current densities are calculated using the projected geometric area of the electrode. As shown in Fig. 6(a), $NiSe_2$-rGO-ST/NF exhibits an oxidation peak around 1.35 V *vs.* RHE before H_2O oxidation, which is attributed to the transformation of Ni^{II} to Ni^{III} species.[101,102] The linear polarization curve (LSV) without *iR* correction for the electrocatalysts for OER is shown in Fig. S3(b).† The overpotential is affected by metal insertion in the MSe_x-rGO-ST/NF electrocatalyst. $FeSe_2$-rGO/NF demonstrated significantly better OER performance than RuO_x/NF, $NiSe_2$-rGO-ST/NF, and $CoSeO_3$-rGO-ST/NF, with overpotential at

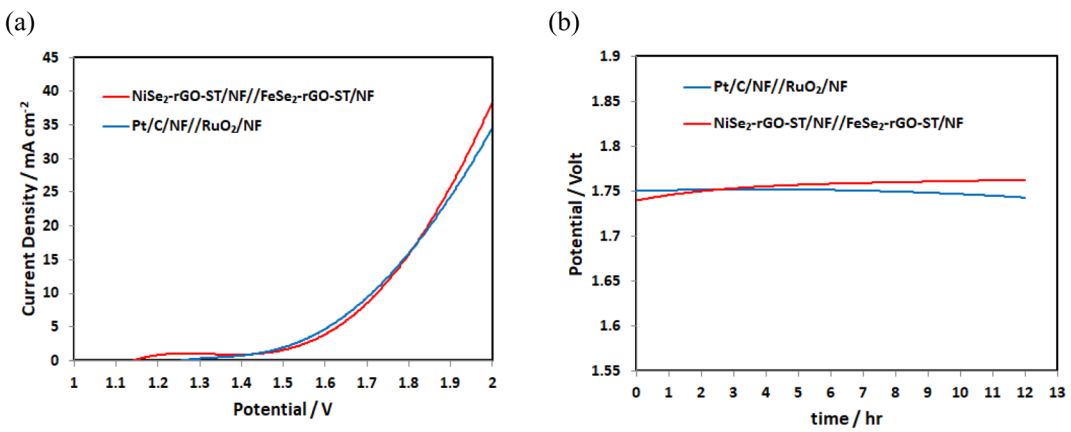

Fig. 7 (a) LSV curves of Pt/C/NF||RuO_2/NF and $NiSe_2$-rGO-ST/NF||$FeSe_2$-rGO-ST/NF, (b) the chronoamperometry curve of Pt/C/NF||RuO_2/NF and $NiSe_2$-rGO-ST/NF||$FeSe_2$-rGO-ST/NF at 10 mA cm^{-2}.

20 mA cm^{-2} of 270, 229, 280, and 284, respectively. At 50 mA cm^{-2}, the overpotential for RuO_x/NF, $FeSe_2$-rGO/NF, $NiSe_2$-rGO-ST/NF, and $CoSeO_3$-rGO-ST/NF are 325, 297, 400, and 475, respectively as shown in Fig. 6(b).

The electrocatalytic performances of $FeSe_2$-rGO-ST/NF for OER in 1 M KOH are compared with previously reported literature. The overpotential value at 10 mA cm^{-2} for different iron composite electrocatalyst *e.g.* $FeSe_2$ supported on CoSe using hydrothermal and selenization process is 183 mV,[29] Fe–Co–S/CC-37.5 and Fe–Co–S/CC-150 using hydrothermal process is 320 mV,[89] Fe–Mo supported on Te is 300 mV,[103] $Fe(Se_{0.5}S_{0.5})_2$ using hydrothermal process is 247 mV,[104] $FeSe_2$ using hydrothermal process is 330 mV,[105] FeP and FeCoNiP prepared by chemical reduction and phosphorization process are 325 and 200 mV, respectively,[106] $Fe_{0.5}Co_{0.5}Se_2$ supported on carbon fiber cloth prepared by solvo thermal and selenization process is 290 mV,[107] $NiFeSe_x$ supported on carbon fiber cloth prepared by electrodeposition followed by solvo thermal process is 310 mV.[108] Additional LSV and Tafel slope comparison of recently published non-noble metal-based for OER catalysts are shown in Table 1.

The kinetics of OER is estimated using corresponding Tafel plots (η *versus* log(j)) for these electrodes (Fig. 6(c)). The Tafel slope for Fe–Se_2-rGO-ST/NF is 106 mV dec^{-1}, which is less than that of RuO_x/NF (117 mV dec^{-1}), $CoSeO_3$-rGO-ST/NF (127 mV dec^{-1}) and Ni–Se_2-rGO-ST/NF (236 Ni–Se_2-rGO-ST), implying a faster OER rate for Fe–Se_2-rGO-ST/NF electrode.

The Nyquist plots (Fig. 6(d)) show that $FeSe_2$-rGO/NF has the smallest charge transfer resistance (R_{ct}) of 4.31 Ω, which is much lower than those of RuO_x/NF (4.685 Ω), $NiSe_2$-rGO-ST/NF (6.627 Ω) and $CoSeO_3$-rGO-ST/NF (4.425 Ω), suggesting its high charge transport efficiency of $FeSe_2$-rGO/NF in OER process.

In order to evaluate the stability of the electrocatalyst, the OER stability is tested by chronoamperometry (CA). Fig. 6(e) shows that all the electrocatalyst indicates negligible deterioration, and better stability during the process of OER after the stability test of 60 h at the current density of 30 mA cm^{-2}.

To determine the precise number of active sites engaged in the electrochemical process, the ESCAs of the electrocatalyst for OER are gathered. The double-layer capacitance (C_{dl}), which is correlated positively with the ESCAs of the catalysts, can be measured at different scan rates in the potential area between (1.2 and 1.3 V *vs.* RHE) to determine the C_{dl} value (Fig. S5†). According to Fig. 6(f), Fe–Se_2-rGO-ST/NF has a substantially higher C_{dl} value (3.46 mF) than other catalysts, which shows that under the same loading situation, Fe–Se_2-rGO-ST/NF has more active sites.

3.4. Water splitting performance

Stimulated by the best performance of the $NiSe_2$-rGO-ST/NF for HER and $FeSe_2$-rGO-ST/NF for OER, the water electrolysis cell is assembled by using $FeSe_2$-rGO-ST/NF as anode and $NiSe_2$-rGO-ST/NF as cathode, for comparison Pt/C/NF and RuO_2/NF is tested as cathode and anode, and the overall water splitting performance is further investigated in 1 M KOH. As shown in Fig. 7(a), the as-assembled $NiSe_2$-rGO-ST/NF||$FeSe_2$-rGO-ST/NF system indicates excellent overall water-splitting performance with low cell voltages of 1.75 V at a current density of 10 mA cm^{-2}, which is close to the value of a noble metal-based electrocatalysts Pt/C/NF||RuO_2/NF. Furthermore, the $NiSe_2$-rGO-ST/NF||$FeSe_2$-rGO-ST/NF system exhibits outstanding electrocatalytic stability with a negligible potential decline at the constant applied current density of 10 mA cm^{-2} for 12 h as shown in Fig. 7(b). The excellent water decomposition activity and stability of $NiSe_2$-rGO-ST/NF||$FeSe_2$-rGO-ST/NF system indicate a promising application potential. The overall water splitting performance is compared with updated published data is listed in Table 1.

4. Conclusion

In conclusion, we have used a simple one-pot solvo thermal method synthesis strategy to construct a bifunctional electrocatalyst of metal selenium nanoparticles (M = Ni, Co & Fe) anchored on the surface of reduced graphene oxide and silica template (rGO-ST). The combined benefits include the improved mass-transport capacity of pores, high conductivity, and an abundance of numerous active sites of $NiSe_2$-rGO-ST and $FeSe_2$-rGO-ST enabling to deliver of remarkable bifunctional catalytic activity towards HER (52.5 mV at 10 mA cm^{-2}), and OER (235 mV at 10 mA cm^{-2}). The assembled electrolyzer with the optimized $NiSe_2$-rGO-ST/NF||$FeSe_2$-rGO-ST/NF electrodes only needs 1.75 V at 10 mA cm^{-2}. The high performance for water splitting is even comparable to those of noble metal catalysts.

Conflicts of interest

There are no conflicts to declare.

Acknowledgements

The work was financially supported by the Science and Technology Development Fund of Egypt (STDF) (Project No. 43149) and the National Key R & D Program of China (Project No. 2021YFE0104700).

References

1 J. Hnát, M. Plevova, R. A. Tufa, J. Zitka, M. Paidar and K. Bouzek, Development and testing of a novel catalyst-coated membrane with platinum-free catalysts for alkaline water electrolysis, *Int. J. Hydrogen Energy*, 2019, **44**, 17493–17504.

2 I. Vincent and D. Bessarabov, Low cost hydrogen production by anion exchange membrane electrolysis: a review, *Renewable Sustainable Energy Rev.*, 2018, **81**, 1690–1704.

3 A. Kongasseri, N. K. Sompalli, V. A. Modak, A. Mohanty and S. Nagarajan, Solid-state ion recognition strategy using 2D hexagonal mesophase silica monolithic platform: a smart two-in-one approach for rapid and selective sensing of Cd^{2+} and Hg^{2+} ions, *Microchim. Acta*, 2020, **187**, 1–13.

4 B. P. Solis, J. C. C. Argüello, L. G. Barba, M. P. Gurrola, Z. Zarhri and D. L. TrejoArroyo, Bibliometric analysis of the mass transport in a gas diffusion layer in PEM fuel cells, *Sustainability*, 2019, **11**(23), 6682.

5 A. Loh, X. Li, O. O. Taiwo, F. Tariq, N. P. Brandon, P. Wang, K. Xu and B. Wang, Development of Ni - Fe based ternary metal hydroxides as highly efficient oxygen evolution catalysts in AEM water electrolysis for hydrogen production, *Int. J. Hydrogen Energy*, 2020, **45**, 24232–24247.

6 E. Fabbri, A. Habereder, K. Waltar, R. Kötz and T. J. Schmidt, Developments and perspectives of oxide-based catalysts for the oxygen evolution reaction, *Catal. Sci. Technol.*, 2014, **4**, 3800–3821.

7 F. Wang, T. A. Shifa, X. Zhan, Y. Huang, K. Liu, Z. Cheng, C. Jiang and J. He, Recent advances in transition-metal dichalcogenide based nanomaterials for water splitting, *Nanoscale*, 2015, **7**, 19764–19788.

8 S. S. Tong, X. J. Wang, Q. C. Li and X. J. Han, Progress on electrocatalysts of hydrogen evolution reaction based on carbon fiber materials, *Chin. J. Anal. Chem.*, 2016, **44**, 1447–1457.

9 M. Ďurovič, J. Hnát and K. Bouzek, Electrocatalysts for the hydrogen evolution reaction in alkaline and neutral media. A comparative review, *J. Power Sources*, 2021, **493**, 229708.

10 L. Yang, H. Qi, C. Zhang and X. Sun, An efficient bifunctional electrocatalyst for water splitting based on cobalt phosphide, *Nanotechnology*, 2016, **27**, 23LT01.

11 G. Li, S. Li, J. Ge, C. Liu and W. Xing, Discontinuously covered IrO_2-RuO_2@Ru electrocatalysts for the oxygen evolution reaction: how high activity and long-term durability can be simultaneously realized in the synergistic and hybrid nano-structure, *J. Mater. Chem. A*, 2017, **5**, 17221–17229.

12 T. H. Wondimu, G. C. Chen, D. M. Kabtamu, H. Y. Chen, A. W. Bayeh, H. C. Huang and C. H. Wang, Highly efficient and durable phosphine reduced iron-doped tungsten oxide/reduced graphene oxide nanocomposites for the hydrogen evolution reaction, *Int. J. Hydrogen Energy*, 2018, **43**, 6481–6490.

13 J. Yang, C. Cai, Y. Li, L. Gao, H. Guo, B. Wang, B. Pu and X. Niu, *In situ* cobalt and nitrogen doped mesoporous graphitic carbon electrocatalyst *via* directly pyrolyzing hyperbranched cobalt phthalocyanine for hydrogen evolution reaction, *Electrochim. Acta*, 2018, **262**, 48–56.

14 M. A. Pellow, C. J. M. Emmott, C. J. Barnhart and S. M. Benson, Hydrogen or batteries for grid storage? A net energy analysis, *Energy Environ. Sci.*, 2015, **8**, 1938–1952.

15 F. Song, L. Bai, S. Lee, C. Hu, L. Liardet, X. Hu, F. Song, L. Bai, A. Moysiadou, S. Lee, C. Hu and L. Liardet, Transition metal oxides as electrocatalysts for the oxygen evolution reaction in alkaline solutions : an application-inspired renaissance, *J. Am. Chem. Soc.*, 2018, **140**(25), 7748–7759.

16 Z. Cai, X. Bu, P. Wang, J. C. Ho, J. Yang and X. Wang, Recent advances in layered double hydroxide electrocatalysts for the oxygen evolution reaction, *J. Mater. Chem. A*, 2019, **7**, 5069–5089.

17 H. Wang, S. Zhu, J. Deng, W. Zhang, Y. Feng and J. Ma, Transition metal carbides in electrocatalytic oxygen evolution reaction, *Chin. Chem. Lett.*, 2021, **32**, 291–298.

18 M. Jiang, J. Li, J. Li, Y. Zhao, L. Pan, Q. Cao, D. Wang and Y. Du, Two-dimensional bimetallic phosphide ultrathin nanosheets as non-noble electrocatalysts for a highly efficient oxygen evolution reaction, *Nanoscale*, 2019, **11**, 9654–9660.

19 M. Cui, C. Yang, B. Li, Q. Dong, M. Wu, S. Hwang, H. Xie, X. Wang, G. Wang and L. Hu, High-entropy metal sulfide nanoparticles promise high-performance oxygen evolution reaction, *Adv. Energy Mater.*, 2021, **11**, 2002887.

20 J. Huang, Y. Jiang, T. An and M. Cao, Increasing the active sites and intrinsic activity of transition metal chalcogenide electrocatalysts for enhanced water splitting, *J. Mater. Chem. A*, 2020, **8**, 25465–25498.

21 M. I. Mejía, J. M. Marín, G. Restrepo, L. A. Rios, C. Pulgarín and J. Kiwi, Preparation, testing and performance of a TiO_2/polyester photocatalyst for the degradation of gaseous methanol, *Appl. Catal., B*, 2010, **94**, 166–172.

22 R. P. Cavalcante, R. F. Dantas, B. Bayarri, O. González, J. Giménez, S. Esplugas and A. Machulek, Synthesis and characterization of B-doped TiO_2 and their performance for the degradation of metoprolol, *Catal. Today*, 2015, **252**, 27–34.

23 X. Chen, X. Wang, X. Zhang, D. Liu, K. Srinivas, F. Ma, B. Wang, B. Yu, Q. Wu and Y. Chen, Facile and scalable synthesis of heterostructural $NiSe_2$/$FeSe_2$ nanoparticles as efficient and stable binder-free electrocatalyst for oxygen evolution reaction, *Int. J. Hydrogen Energy*, 2021, **46**, 35198–35208.

24 H. Zhang, L. Chao Nengzi, B. Li, Q. Cheng, J. Gou and X. Cheng, Successfully synthesis of $FeSe_2$/$CoFe_2O_4$ heterojunction with high performance for hydrogen evolution reaction, *Renewable Energy*, 2020, **155**, 717–724.

25 L. Zhai, C. H. Mak, J. Qian, S. Lin and S. P. Lau, Self-reconstruction mechanism in $NiSe_2$ nanoparticles/carbon fiber paper bifunctional electrocatalysts for water splitting, *Electrochim. Acta*, 2019, **305**, 37–46.

26 C. Zhang, Y. Zhang, S. Zhou and C. Li, Self-supported iron-doping $NiSe_2$ nanowrinkles as bifunctional electrocatalysts for electrochemical water splitting, *J. Alloys Compd.*, 2020, **818**, 152833.

27 J. Yu, W. J. Li, G. Kao, C. Y. Xu, R. Chen, Q. Liu, J. Liu, H. Zhang and J. Wang, In-situ growth of CNTs encapsulating P-doped $NiSe_2$ nanoparticles on carbon framework as efficient bifunctional electrocatalyst for overall water splitting, *J. Energy Chem.*, 2021, **60**, 111–120.

28 F. Kong, J. Zheng, S. Tao and B. Qian, Electrochemical and electrocatalytic performance of $FeSe_2$ nanoparticles improved by selenium matrix, *Mater. Lett.*, 2021, **284**, 128947.

29 X. Xing, C. Wu, G. Yang, T. Tong, Y. Wang, D. Wang, F. C. Robles Hernandez, Z. Ren, Z. Wang and J. Bao, $FeSe_2$/CoSe nanosheets for efficient overall water splitting

under low cell voltages, *Mater. Today Chem.*, 2022, **26**, 101110.

30 B. Sun, G. Dong, J. Ye, D. feng Chai, X. Yang, S. Fu, M. Zhao, W. Zhang and J. Li, Selenium anion substitution endows manganese sulfide as a bifunctional electrocatalyst for efficient water splitting in alkaline solutions, *Chem. Eng. J.*, 2023, **459**, 141610.

31 X. Pan, W. He, D. Cao, Y. Li, C. Liu, L. Liang, Q. Hao and H. Liu, Engineering selenium vacancies on $CoSe_2$ nanoarrays for alkaline hydrogen evolution, *ACS Appl. Nano Mater.*, 2023, **6**, 1724–1731.

32 J. N. Hausmann and P. W. Menezes, Why should transition metal chalcogenides be investigated as water splitting precatalysts even though they transform into (oxyhydr) oxides?, *Curr. Opin. Electrochem.*, 2022, **34**, 100991.

33 Y. Huang, C. Lee, H. Pang, C. Li, M. Fan, R. Vittal and K. Ho, Microemulsion-controlled synthesis of $CoSe_2$/$CoSeO_3$ composite crystals for electrocatalysis in dye-sensitized solar cells, *Mater. Today*, 2017, **6**, 189–197.

34 D. J. Zhao, S. Y. Ma and G. P. Yin, Preparation of $CoSeO_3$ compound and its catalytic performance for cathodic oxygen reduction, *Int. J. Inorg. Mater.*, 2013, **28**, 644–648.

35 Y. Zhou, Y. Wu, D. Guo, J. Li, G. Dong, D.-F. Chai, X. Yang, S. Fu and G. Sui, Sulfur vacancy modulated nickel-doped Co_4S_3 hollow nanocube/nitrogen-doped V_2CT_xMXene nanosheet composites for optimizing the hydrogen evolution reaction, *Mater. Chem. Front.*, 2023, **7**, 306–314.

36 C. Zhao, P. Li, D. Shao, R. Zhang, S. Wang, Z. Zhu and C. Zhao, Phytic acid-derived Co_{2-x} $NixP_2O_7$-C/RGO and its superior OER electrocatalytic performance, *Int. J. Hydrogen Energy*, 2019, **44**, 844–852.

37 G. S. Y. Xu, K. Sheng and C. Li, Self-assembled graphene hydrogel *via* a one-step, *ACS Nano*, 2010, **4**, 4324–4330.

38 Y. Bao, C. Shi, T. Wang, X. Li and J. Ma, Recent progress in hollow silica: template synthesis, morphologies and applications, *Microporous Mesoporous Mater.*, 2016, **227**, 121–136.

39 Z. Teng, Y. Han, J. Li, F. Yan and W. Yang, Preparation of hollow mesoporous silica spheres by a sol–gel/emulsion approach, *Microporous Mesoporous Mater.*, 2010, **127**, 67–72.

40 S. E. Lowe, G. Shi, Y. Zhang, J. Qin, L. Jiang, S. Jiang, M. Al-Mamun, P. Liu, Y. L. Zhong and H. Zhao, The role of electrolyte acid concentration in the electrochemical exfoliation of graphite: mechanism and synthesis of electrochemical graphene oxide, *Nano Mater. Sci.*, 2019, **1**, 215–223.

41 W. Guoxiu, Y. Juan, P. Jinsoo, G. Xinglong, W. Bei, L. Hao and Y. Jane, Facile synthesis and characterization of graphene nanosheets, *J. Phys. Chem. C*, 2008, **112**, 8192–8195.

42 Y. Z. N. Htwe, W. S. Chow, Y. Suda, A. A. Thant and M. Mariatti, Effect of electrolytes and sonication times on the formation of graphene using an electrochemical exfoliation process, *Appl. Surf. Sci.*, 2019, **469**, 951–961.

43 S. S. Sheshmani and M. A. Fashapoyeh, Suitable chemical methods for preparation of graphene oxide, graphene and surface functionalized graphene nanosheets – PubMed, *Acta Chim. Slov.*, 2013, **60**, 813–825.

44 H. Sun, G. Xu, W. Lian, G. Kastiukas, J. Zhang, X. Zhang, W. Liu, F. Xing and J. Ren, Electrochemical synthesis and property characterisation of graphene oxide using water as electrolyte, *Chem. Phys. Lett.*, 2022, **786**, 139206.

45 G. Konstantopoulos, E. Fotou, A. Ntziouni, K. Kordatos and C. A. Charitidis, A systematic study of electrolyte effect on exfoliation efficiency and green synthesis of graphene oxide, *Ceram. Int.*, 2021, **47**, 32276–32289.

46 Y. Sunwoo, G. Karunakaran and E. B. Cho, Hollow mesoporous silica nanospheres using pentablock copolymer micelle templates, *Ceram. Int.*, 2021, **47**, 13351–13362.

47 C. Decarpigny, R. Bleta, A. Ponchel and E. Monflier, Oxidation of 2,5-diformfylfuran to 2,5-furandicarboxylic acid catalyzed by Candida antarctica Lipase B immobilized in a cyclodextrin-templated mesoporous silica. The critical role of pore characteristics on the catalytic performance, *Colloids Surf., B*, 2021, **200**, 111606.

48 W. Lu, A. T. Tarekegne, Y. Ou, S. Kamiyama and H. Ou, Temperature-dependent photoluminescence properties of porous fluorescent SiC, *Sci. Rep.*, 2019, **9**, 16333.

49 T. Wu, Y. Wang, H. Zhao, J. Dong and J. Xu, Si doped Fe-N/C catalyst for oxygen reduction reaction directed by ordered mesoporous silica nanospheres template strategy, *J. Colloid Interface Sci.*, 2021, **603**, 706–715.

50 X. Xiong, J. Zhang, Y. Cheng, C. Chen, J. Zeng, J. Xi, Z. Kong, Y. J. Yuan and Z. Ji, Excellent photocatalytic and photoelectrochemical activities from 1D/2D $FeSe_2$/SnSe heterojunction photocatalysts constructed by $FeSe_2$ nanorods and SnSe nanosheets, *Int. J. Hydrogen Energy*, 2022, **47**, 7189–7201.

51 J. Wang, S. Sarwar, J. Song, L. Du, T. Li, Y. Zhang, B. Li, Q. Guo, J. Luo and X. Zhang, One-step microwave synthesis of self-supported $CoSe_2$@$NiSe_2$ nanoflowers on 3D nickel foam for high performance supercapacitors, *J. Alloys Compd.*, 2022, **892**, 162079.

52 J. Dong, J. Wu, J. Jia, L. Fan, Z. Lan, J. Lin and Y. Wei, Cobalt selenite dihydrate as an effective and stable Pt-free counter electrode in dye-sensitized solar cells, *J. Power Sources*, 2016, **336**, 83–90.

53 B. Yu, F. Qi, Y. Chen, X. Wang, B. Zheng, W. Zhang, Y. Li and L. C. Zhang, Nanocrystalline $Co_{0.85}Se$ anchored on graphene nanosheets as a highly efficient and stable electrocatalyst for hydrogen evolution reaction, *ACS Appl. Mater. Interfaces*, 2017, **9**, 30703–30710.

54 S. Xu, Z. Lei and P. Wu, Facile preparation of 3D MoS_2/$MoSe_2$ nanosheet–graphene networks as efficient electrocatalysts for the hydrogen evolution reaction, *J. Mater. Chem. A*, 2015, **3**, 16337–16347.

55 M. Zhu, Q. Yan, Q. Lu, Y. Xue, Y. Yan, J. Yin, K. Zhu, K. Cheng, K. Ye, J. Yan, D. Cao and G. Wang, Iron-doped NiSe2 in-situ grown on graphene as an efficient electrocatalyst for oxygen evolution reaction, *J. Electroanal. Chem.*, 2020, **866**, 114134.

56 K. Kaviyarasu, L. Kotsedi, A. Simo, X. Fuku, F. T. Thema, K. Anand, K. G. Moodley, J. Kennedy and M. Maaza, Quantum phenomena of ZnSe nanocrystals prepared by electron beam evaporation technique, *Funct. Nanostruct.*, 2017, 73–83.

57 B. Balamuralitharan, S. N. Karthick, S. K. Balasingam, K. V. Hemalatha, S. Selvam, J. Anandha Raj, K. Prabakar, Y. Jun and H.-J. Kim, Hybrid reduced graphene oxide/$MnSe_2$ cubes: a new electrode material for supercapacitors, *Energy Technol.*, 2017, **5**(1), 1953–1962.

58 S. Nouseen, P. Singh, S. Lavate, J. Chattopadhyay, A. M. Kuchkaev, D. G. Yakhvarov and R. Srivastava, Transition metal based ternary hierarchical metal sulphide microspheres as electrocatalyst for splitting of water into hydrogen and oxygen fuel, *Catal. Today*, 2022, **397–399**, 618–630.

59 T. Feng, J. Jin, Y. Cao, H. Li, B. Dong and L. Cao, A novel $CoSeO_3$ photocatalyst assisting g-C_3N_4 in enhancing hydrogen evolution through Z scheme mode, *Int. J. Hydrogen Energy*, 2022, **47**, 5999–6010.

60 D. S. Han, B. Batchelor and A. Abdel-wahab, XPS analysis of sorption of selenium(IV) and selenium (VI) to mackinawite (FeS), *Environ. Prog. Sustainable Energy*, 2011, 1–10.

61 C. Cui, Z. Wei, G. Zhou, W. Wei, J. Ma and L. Chen, Quasi-reversible conversion reaction of $CoSe_2$/nitrogen-doped carbon nanofiber towards long-lifetime anode materials for sodium-ion batteries, *J. Mater. Chem.*, 2018, **A6**, 7088–7098.

62 Y. Wu, S. Chen, Y. Weng, Y. Zhang, C. Wu, L. Sun, S. Zhang and Q. Yan, Facile synthesis and color conversion of Cu – doped ZnSe quantum dots in an aqueous solution, *J. Mater. Sci. Mater. Electron.*, 2019, **30**, 21406–21415.

63 R. Yan, D. Gauthier, G. Flamant and Y. Wang, Behavior of selenium in the combustion of coal or coke spiked with Se, *Combust. Flame*, 2004, **138**, 20–29.

64 Y. Gong, W. Ding, Z. Li, R. Su, X. Zhang, J. Wang, J. Zhou, Z. Wang, Y. Gao, S. Li, P. Guan, Z. Wei and C. Sun, An inverse spinel cobalt-iron oxide and N-doped graphene composite as an efficient and durable bifuctional catalyst for Li-O_2 batteries an inverse spinel cobalt-iron oxide and N-doped graphene composite as an efficient and durable bifuctional catalyst for, *ACS Catal. Introd.*, 2018, 1–25.

65 L. Wen, X. Zhang, J. Liu, X. Li, C. Xing and X. Lyu, Cr-dopant induced breaking of scaling relations in CoFe layered double hydroxides for improvement of oxygen evolution reaction, *Small*, 2019, **15**(35), 1902373.

66 L. Cao, Y. Hu, S. Tang, A. Iljin, J. Wang, Z. Zhang and T. Lu, Fe-CoP electrocatalyst derived from a bimetallic prussian blue analogue for large-current-density oxygen evolution and overall water splitting, *Adv. Sci.*, 2018, **5**(10), 1800949.

67 X. Zhao, Y. Fan, H. Wang, C. Gao, Z. Liu, B. Li, Z. Peng, J. Yang and B. Liu, Cobalt phosphide-embedded reduced graphene oxide as a bifunctional catalyst for overall water splitting, *Am. Chem. Soc.*, 2020, **5**(12), 6516–6522.

68 R. D. Desautels, J. W. Freeland, M. P. Rowe and J. Van Lierop, The role of interfacial metal silicates on the magnetism in FeCo/SiO_2, *J. Appl. Phys.*, 2015, **728**, 2–6.

69 Peter C. J. Graat and M. A. J. Somers, Simultaneous determination of composition and thickness of thin iron-oxide films from XPS Fe 2p spectra, *Appl. Surf. Sci.*, 1996, **100**, 36–40.

70 S. Xie, J. Gou, B. Liu and C. Liu, Nickel-cobalt selenide as high-performance and long-life electrode material for supercapacitor, *J. Colloid Interface Sci.*, 2019, **540**, 306–314.

71 A. Sivanantham and S. Shanmugam, Nickel selenide supported on nickel foam as an efficient and durable non-precious electrocatalyst for the alkaline water electrolysis, *Appl. Catal., B*, 2017, **203**, 485–493.

72 J. Wang, Q. Zhao, H. Hou, Y. Wu, W. Yu, X. Ji and L. Shao, Honeycomb-like carbon frameworks for e ff ective methanol oxidation, *RSC Adv.*, 2017, 14152–14158.

73 P. Salunkhe, A. V. Muhammed Ali and D. Kekuda, Investigation on tailoring physical properties of nickel oxide thin films grown by dc magnetron sputtering Investigation on tailoring physical properties of nickel oxide thin films grown by dc magnetron sputtering, *Mater. Res. Express*, 2020, **7**, 016427.

74 J. K. Kim, PEG-assisted sol-gel synthesis of compact nickel oxide hole-selective layer with modified interfacial properties for organic solar cells, *Polymers*, 2019, **11**(1), 120.

75 D. Soo Kim and H. Chul Lee, Nickel vacancy behavior in the electrical conductance of nonstoichiometric nickel oxide film, *J. Appl. Phys.*, 2012, **112**, 034504.

76 K. Ao, J. Dong, C. Fan, D. Wang, Y. Cai, D. Li, F. Huang and Q. Wei, Formation of yolk-shelled nickel-cobalt selenide dodecahedral nanocages from metal-organic frameworks for efficient hydrogen and oxygen evolution formation of yolk-shelled nickel–cobalt selenide dodecahedral nanocages from metal–organic frameworks for eff, *ACS Sustainable Chem. Eng.*, 2018, 1–28.

77 H. Chen, S. Chen, M. Fan, C. Li, D. Chen and G. Tian, Bimetallic nickel cobalt selenides: a new kind of electroactive material for high-power energy storage, *J. Mater. Chem. A*, 2015, **3**, 23653–23659.

78 B. Yu, F. Qi, Y. Chen, X. Wang, B. Zheng, W. Zhang, Y. Li and L. Zhang, Efficient and stable electrocatalyst for hydrogen evolution reaction nanocrystalline $Co_{0.85}Se$ anchored on graphene nanosheets as a highly efficient and stable electrocatalyst for hydrogen evolution reaction, *ACS Appl. Mater. Interfaces*, 2017, 1–29.

79 Y. Kumar, A. Sharma, A. Ahmed, C. K. Hong and P. M. Shirage, Morphology-controlled synthesis and enhanced energy product (BH)max of $CoFe_2O_4$ nanoparticles, *New J. Chem.*, 2018, **42**(19), 15793–15802.

80 K. Hwa, A. Ganguly, A. Santhan, T. Sanjay and K. Sharma, Vanadium selenide decorated reduced graphene oxide nanocomposite: a co-active catalyst for the detection of 2,4,6-trichloropheno, *Chemosphere*, 2021, **282**, 130874.

81 Z. Liu, N. Li, H. Zhao and Y. Du, Colloidally synthesized $MoSe_2$/graphene hybrid nanostructures as efficient electrocatalysts for hydrogen evolution, *J. Mater. Chem. A*, 2015, **3**, 19706–19710.

82 W. Xu and H. Wang, Earth – abundant amorphous catalysts for electrolysis of water, *Chin. J. Catal.*, 2017, **38**, 991–1005.

83 T. H. Wondimu, G. Chen, D. M. Kabtamu, H. Chen, A. W. Bayeh, H. Huang and C. Wang, Selenium vacancy and phosphorus-doping- induced phase transition engineering of cobalt diselenide as bi-functional catalyst for water electrolysis, *Int. J. Hydrogen Energy*, 2019, **44**, 28566–28577.

84 N. R. Elezovi, G. Brankovi, P. Zabinski, M. Marzec and V. D. Jovi, Ultra-thin layers of iridium electrodeposited on Ti_2AlC support as cost effective catalysts for hydrogen production by water electrolysis, *J. Electroanal. Chem.*, 2020, **878**, 114575.

85 K. R. Park, D. T. Tran, T. T. Nguyen, N. H. Kim and J. H. Lee, Copper-incorporated heterostructures of amorphous $NiSe_x$/Crystalline $NiSe_2$ as an efficient electrocatalyst for overall water splitting, *Chem. Eng. J.*, 2021, **422**, 130048.

86 X. Peng, Y. Yan, S. Xiong, Y. Miao, J. Wen, Z. Liu, B. Gao, L. Hu and P. K. Chu, Se-$NiSe_2$ hybrid nanosheet arrays with self-regulated elemental Se for efficient alkaline water splitting, *J. Mater. Sci. Technol.*, 2022, **118**, 136–143.

87 M. Islam, D. T. Tran, T. H. Nguyen, V. A. Dinh, N. H. Kim and J. H. Lee, Efficient synergism of NiO-$NiSe_2$ nanosheet-based heterostructures shelled titanium nitride array for robust overall water splitting, *J. Colloid Interface Sci.*, 2022, **612**, 121–131.

88 X. Wang, P. Zhao, L. Ling, Y. Luo, Z. Li, Z. Jiao and L. Cheng, Optimizing the electronic structure of $NiSe_2$/$CoSe_2$ nanosheet arrays by phosphorus doping for high-efficiency oxygen evolution electrocatalysts, *J. Alloys Compd.*, 2022, **927**, 166845.

89 X. Li, F. Duan, M. Deng, W. Zheng, Y. Lin, Y. Dan, X. Cheng and L. Chen, Effect of Fe doping on Co-S/carbon cloth as bifunctional electrocatalyst for enhanced water splitting, *J. Electroanal. Chem.*, 2022, **922**, 116723.

90 S. Naik Shreyanka, J. Theerthagiri, S. J. Lee, Y. Yu and M. Y. Choi, Multiscale design of 3D metal–organic frameworks (M−BTC, M: Cu, Co, Ni) *via* PLAL enabling bifunctional electrocatalysts for robust overall water splitting, *Chem. Eng. J.*, 2022, **446**, 137045.

91 Y. Zheng, Y. Jiao, M. Jaroniec and S. Z. Qiao, Advancing the electrochemistry of the hydrogen-evolution reaction through combining experiment and theory, *Angew. Chem., Int. Ed. Engl.*, 2015, **54**, 52–65.

92 H. Zhu, M. L. Du, M. Zhang, M. L. Zou, T. T. Yang, S. L. Wang, J. M. Yao and B. C. Guo, S-rich single-layered MoS2 nanoplates embedded in N-doped carbon nanofibers: efficient co-electrocatalysts for the hydrogen evolution reaction, *Chem. Commun.*, 2014, **50**, 15435–15438.

93 L. Zeng, K. Sun, X. Wang, Y. Liu, Y. Pan, Z. Liu, D. Cao, Y. Song, S. Liu and C. Liu, Three-dimensional-networked Ni_2P/Ni_3S_2 heteronanoflake arrays for highly enhanced electrochemical overall-water-splitting activity, *Nano Energy*, 2018, **51**, 26–36.

94 X. Zhang, J. Li, Y. Yang, S. Zhang, H. Zhu, X. Zhu, H. Xing, Y. Zhang, B. Huang, S. Guo and E. Wang, Co_3O_4/$Fe_{0.33}Co_{0.66}P$ interface nanowire for enhancing water oxidation catalysis at high current density, *Adv. Mater.*, 2018, **30**(45), 1803551.

95 X. Xie, R. Yu, N. Xue, A. Bin Yousaf, H. Du, K. Liang, N. Jiang and A. W. Xu, P doped molybdenum dioxide on Mo foil with high electrocatalytic activity for the hydrogen evolution reaction, *J. Mater. Chem. A*, 2016, **4**, 1647–1652.

96 J. D. Benck, Z. Chen, L. Y. Kuritzky, A. J. Forman and T. F. Jaramillo, Amorphous molybdenum sulfide catalysts for electrochemical hydrogen production: insights into the origin of their catalytic activity, *ACS Catal.*, 2012, **2**, 1916–1923.

97 P. Stelmachowski, A. H. A. Monteverde Videla, K. Ciura and S. Specchia, Oxygen evolution catalysis in alkaline conditions over hard templated nickel–cobalt based spinel oxides, *Int. J. Hydrogen Energy*, 2017, **42**, 27910–27918.

98 M. A. Lukowski, A. S. Daniel, C. R. English, F. Meng, A. Forticaux, R. J. Hamers and S. Jin, Highly active hydrogen evolution catalysis from metallic WS2 nanosheets, *Energy Environ. Sci.*, 2014, **7**, 2608–2613.

99 Y. Ito, W. Cong, T. Fujita, Z. Tang and M. Chen, High catalytic activity of nitrogen and sulfur co-doped nanoporous graphene in the hydrogen evolution reaction, *Angew. Chem., Int. Ed. Engl.*, 2015, **54**, 2131–2136.

100 J. Zhu, Z. Liu, M. Zhai and Y. Ni, $Ni_{1-x}Co_xSe$ nanostructures deposited on nickel foam by a facile potentiostatic route for enhanced OER performance, *J. Phys. Chem. Solids*, 2021, **148**, 109658.

101 C. Tang, N. Cheng, Z. Pu, W. Xing and X. Sun, NiSe nanowire film supported on nickel foam: an efficient and stable 3D bifunctional electrode for full water splitting, *Angew. Chem., Int. Ed.*, 2015, **54**, 9351–9355.

102 S. Guan, X. Fu, Z. Lao, C. Jin and Z. Peng, NiS-MoS_2 hetero-nanosheet array electrocatalysts for efficient overall water splitting, *Sustain. Energy Fuels*, 2019, **3**, 2056–2066.

103 R. He, M. Li, W. Qiao and L. Feng, Fe doped Mo/Te nanorods with improved stability for oxygen evolution reaction, *Chem. Eng. J.*, 2021, **423**, 130168.

104 Z. Jing, Q. Zhao, D. Zheng, H. Xu, L. Sun, J. Geng, Q. Zhou and J. Lin, Engineering unique $Fe(Se_xS_{1-x})_2$ nanorod bundles for boosting oxygen evolution reaction, *Chem. Eng. J.*, 2021, **418**, 129426.

105 R. Gao, H. Zhang and D. Yan, Iron diselenide nanoplatelets: stable and efficient water-electrolysis catalysts, *Nano Energy*, 2017, **31**, 90–95.

106 J. Xu, J. Li, D. Xiong, B. Zhang, Y. Liu, K. H. Wu, I. Amorim, W. Li and L. Liu, Trends in activity for the oxygen evolution reaction on transition metal (M = Fe, Co, Ni) phosphide pre-catalysts, *Chem. Sci.*, 2018, **9**, 3470–3476.

107 J. Q. Chi, X. Shang, W. K. Gao, B. Dong, K. L. Yan, X. Li, Y. R. Liu, Y. M. Chai and C. G. Liu, Binary metal $Fe_{0.5}Co_{0.5}Se_2$ spheres supported on carbon fiber cloth for efficient oxygen evolution reaction, *Int. J. Hydrogen Energy*, 2017, **42**, 15189–15195.

108 J. Q. Chi, X. Shang, F. Liang, B. Dong, X. Li, Y. R. Liu, K. L. Yan, W. K. Gao, Y. M. Chai and C. G. Liu, Facile synthesis of pyrite-type binary nickel iron diselenides as efficient electrocatalyst for oxygen evolution reaction, *Appl. Surf. Sci.*, 2017, **401**, 17–24.

109 J. Lin, H. Wang, Y. Yan, J. Cao, C. Qu, X. Zheng, J. Feng and J. Qi, Sandwich-like structured $NiSe_2/Ni_2P$@FeP interface nanosheets with rich defects for efficient electrocatalytic water splitting, *J. Power Sources*, 2020, **445**, 227294.

110 Z. Tian, Y. Liu, Q. Xu, Y. Shi, C. Ma, B. Peng, G. Liu, J. Yang and W. Zheng, Fe doped $NiSe_2$ nanoarrays to boost electrocatalytic oxygen evolution reaction, *Electrochim. Acta*, 2022, **425**, 140711.

111 H. Pan, X. Zhang, Y. Jia, Y. Zhang, Z. Jiang, C. Sun, X. Li, L. Zhu and K. Wang, Interfacial composite FeOOH enhanced efficient electrocatalytic oxygen evolution of $NiSe_2/Ni_2O_3$, *J. Alloys Compd.*, 2022, **926**, 166779.

112 W. Li, A. Murisana, Q. Zhang, S. Wang and G. De, Controlled synthesis and M-position regulation of perovskite fluoride KMF3 (M = Co/Fe) with high-efficiency OER performance, *Electrochem. Commun.*, 2022, **141**, 107363.

113 G. Zhang, Z. Li, J. Zeng, L. Yu, C. Zuo, P. Wen, Y. Liu, L. Zhong, H. Chen and Y. Qiu, Ferric ions leached from Fe-based catalyst to trigger the dynamic surface reconstruction of nickel foam for high-efficient OER activity, *Appl. Catal., B*, 2022, **319**, 121921.

114 Y. Liu, P. Ge, Y. Li, X. Zhai, K. Lu, X. Chen, J. Yang, Z. Wang, H. Zhang and G. Ge, Prussian blue analogues derived Fe-NiCoP reveals the cooperation of Fe doping and phosphating for enhancing OER activity, *Appl. Surf. Sci.*, 2023, **615**, 156378.

115 S. Ni, H. Qu, Z. Xu, X. Zhu, H. Xing, L. Wang, J. Yu, H. Liu, C. Chen and L. Yang, Interfacial engineering of the $NiSe_2/FeSe_2$ p–p heterojunction for promoting oxygen evolution reaction and electrocatalytic urea oxidation, *Appl. Catal., B*, 2021, **299**, 120638.

116 S. K. Ramesh, V. Ganesan and J. Kim, $FeSe_2$-$CoSe_2/CoSe_2$ yolk-shell nanoboxes as superior electrocatalysts for the oxygen evolution reaction, *Mater. Lett.*, 2022, **323**, 1–4.

117 X. Lei, X. Xie, K. Sun, S. Liu, T. Hou, H. Peng and G. Ma, Self-generated $FeSe_2$ and $CoSe_2$ nanoparticles confined in N, S-doped porous carbon as efficient and stable electrocatalyst for oxygen evolution reaction, *Electrochim. Acta*, 2023, **445**, 142049.